IEEE Access
Multidisciplinary ⋮ Rapid Review ⋮ Open Access Journal

Received 3 February 2023, accepted 6 March 2023, date of publication 9 March 2023, date of current version 15 March 2023.

Digital Object Identifier 10.1109/ACCESS.2023.3254912

RESEARCH ARTICLE

Indoor Radio Map Construction via Ray Tracing With RGB-D Sensor-Based 3D Reconstruction: Concept and Experiments in WLAN Systems

NORISATO SUGA[1], (Member, IEEE), YOSHIHIRO MAEDA[2], (Member, IEEE), AND KOYA SATO[3], (Member, IEEE)

[1]Department of Information and Communications Engineering, Shibaura Institute of Technology, Tokyo 135-8548, Japan
[2]Department of Electrical Engineering, Tokyo University of Science, Tokyo 125-8585, Japan
[3]Artificial Intelligence eXploration Research Center, The University of Electro-Communications, Tokyo 182-8585, Japan

Corresponding author: Koya Sato (k_sato@ieee.org)

The work of Norisato Suga was supported in part by the Telecommunications Advancement Foundation, and in part by the Environment Research and Technology Development Fund of the Environmental Restoration and Conservation Agency of Japan under Grant JPMEERF20222M01. The work of Yoshihiro Maeda was supported in part by the Environment Research and Technology Development Fund of the Environmental Restoration and Conservation Agency of Japan under Grant JPMEERF20222M01. The work of Koya Sato was supported by the Japan Science and Technology Agency (JST), ACT-X, JPMJAX21AA.

ABSTRACT This paper proposes an RGB-D sensor-aided ray-tracing simulation framework for indoor radio map construction that models indoor information, such as walls and obstacles, as a set of cuboids. Radio maps can accelerate indoor wireless systems, including resource optimization and fingerprint-based localization. We can construct an accurate radio map using a ray-tracing algorithm with precise indoor structures and obstacles information. However, it is challenging to acquire this indoor information because manual observations of these are expensive. To mitigate this critical drawback, we propose utilizing three-dimensional information obtained from RGB-D images for ray-tracing simulation. The proposed method semi-automatically models indoor information as cuboids from three-dimensional information with RGB-D images. The proposed method then feeds these cuboids into a ray-tracing simulation. Indoor experiments using wireless LANs over 5180 and 2452 MHz clarified that the proposed method accurately constructs the radio map.

INDEX TERMS Radio map construction, RGB-D sensor, 3D reconstruction, point cloud.

I. INTRODUCTION

Radio maps visualize the average received signal power values [1]. Although related discussions were initiated in the field of dynamic spectrum sharing [2], [3], [4], [5], recent results have shown their advances in various indoor wireless applications, such as wireless resource optimization [6], [7], [8], localization [9], [10], [11], [12], [13], [14], [15], and navigation [16]. Because the accuracy of radio maps affects the performance of these applications, it is crucial to develop an accurate radio map construction method.

Radio map construction methods can be categorized into (a) crowdsensing-based and (b) simulation-based approaches. In the crowdsensing-based approach, mobile terminals feedback the received signal power values to a centralized server. The received power information of the entire area is subsequently estimated by grid-averaging the observation results and performing spatial interpolation (e.g., Kriging [17]). However, the accuracy of this approach relies on the shadowing correlation distance. Because indoor channels tend to exhibit a short-range correlation distance [18], this approach does not necessarily yield an accurate radio map [19].

Simulation-based approaches include empirical model-based methods [20] and ray-tracing simulations [21]. The empirical model-based approach can approximately estimate a radio map with low complexity; however, its accuracy is limited owing to the difficulty in estimating the shadowing

The associate editor coordinating the review of this manuscript and approving it for publication was Kashif Saleem.

TABLE 1. Classification of radio map construction methods.

Approach	Pros	Cons
Empirical path loss model	It can estimate the radio environment with low complexity and no sensing cost requirements.	It is difficult to estimate shadowing factor and limits the estimation accuracy, specifically in indoor scenarios.
Ray tracing simulation	Accurate estimation for both indoor/outdoor scenarios.	It requires precise information on structures and obstacles.
Crowdsensing with Kriging	Optimal estimation in outdoor scenarios. Its accuracy can be enhanced as the number of measurements increases.	Its accuracy depends on spatial correlation distance. Further, it is challenging to obtain sensing locations in indoor situations.

factors. In contrast, ray tracing can be used to construct a highly accurate radio map that reflects the effects of structures and obstacles.

However, the ray-tracing-based approach requires precise information about indoor environments, such as wall size, furniture deployment, and other obstacles. Although each piece of structural and obstacle information significantly affects the received-power performance, obtaining this information manually is impractical because of the large number of elements (e.g., desks, chairs, and computers) and their rearrangements, which increases the cost of this approach.

To make indoor radio map construction more tractable and accurate, in this paper, we propose an RGB-depth (RGB-D) sensor-assisted ray-tracing simulation approach for indoor radio map construction. The proposed method uses an RGB-D sensor to model the indoor information as a set of cuboids. To this end, the colored point clouds are acquired in advance. After PointNet++ [22] labels semantics to the point clouds, the indoor information is modeled as a set of cuboids that can immediately be used for the ray-tracing simulation.

The major contributions of this study are summarized as follows:

- We develop an image sensor-assisted indoor radio-propagation simulation framework based on 3D reconstruction for MHz-GHz systems.
- We demonstrate the proposed method for indoor wireless local area network (WLAN) scenarios over 5180 and 2452 MHz bands. The experimental results show that our approach can accurately construct the radio map based on the 3D reconstruction.
- Furthermore, based on the experimental results, we reveal that the proposed method can construct radio maps with better accuracy than received signal power value sensing with Kriging.

The remainder of this paper is organized as follows. We first review related works in Section II. Subsequently, Section III gives the proposed RGB-D sensor-aided radio map construction framework. The measurement configuration is detailed in Section IV, and we present the performance evaluation results in Section V. Finally, Section VI concludes this work. Note that major notations are listed in Table 2.

II. RELATED WORKS ON RADIO MAP CONSTRUCTION

There has been a wide range of discussions on radio map construction. Discussions on radio map construction had been initiated in the early 2000s with the term *radio environment map* (REM) in dynamic spectrum access (DSA) [23]. DSA systems must obtain white space information to decide their communication strategy; however, node-alone spectrum sensing tends to exhibit a low-accuracy white space detection owing to multipath fading. REM has been introduced as side information to (and accurately) detect white spaces. By storing REMs in a cloud server, DSA systems allow nodes to estimate spectrum-sharing opportunities with limited spectrum-sensing capability. Its discussions have been conducted on outdoor television white space (TVWS) systems.

REM-based DSA systems have been implemented in spectrum databases for TVWS in various countries [24]. The spectrum database constructs white space information estimated by empirical path loss models.[1] However, several studies have highlighted that such empirical path loss model-based REM construction limits accuracy. In [25], the authors

TABLE 2. Major notations.

Notation	Description
I_i	The i-th RGB image
D_i	The i-th depth image
K	Number of images
$\mathcal{P}_i$	The i-th point cloud corresponding to I_i and D_i
$\boldsymbol{T}$	Rotation and translation parameters in ICP algorithm
$\xi(\cdot,\cdot)$	Distance function of the points
$\mathcal{K}$	Set of pairs of points corresponding to $\mathcal{P}$ and $\mathcal{Q}$
$\mathcal{P}^M$	The integrated 3D point-cloud model
$d_{\min}$	Minimum density threshold in point-cloud down sampling
$\mathcal{L}$	Set of output labels in semantic segmentation
$\mathcal{P}^S$	Semantic-segmented point-cloud data
a, b, c, d	Parameters in plane equation (Eq. (2))
$\|\cdot\|_2$	ℓ^2 norm operator
N	Number of planes
$\mathcal{P}_i^F$	The i-th point clouds for walls, ceilings and floors
$\mathcal{P}_i^R$	The i-th point clouds for objects
$\mathcal{C}_i^F$	The i-th cuboids for walls, ceilings and floors
$\mathcal{C}_i^R$	The i-th cuboids for objects
$\mathcal{D}$	Dataset for received signal power values
$\boldsymbol{x}_j$	Measurement location
$P(\boldsymbol{x})$	Received signal power at $\boldsymbol{x}$
$\hat{P}(\boldsymbol{x})$	Estimation result for $P(\boldsymbol{x})$
P_{Tx}	Transmission power
η	Path loss index
$\boldsymbol{x}_{\mathrm{Tx}}$	Transmission location
$W(\boldsymbol{x})$	Shadowing at $\boldsymbol{x}$
ω_i	Weighting factor in Kriging
n	Datasize in $\mathcal{D}$
n_{test}	Number of test points in RMSE analysis

[1] For example, spectrum database in the US estimated the white spaces based on *F-curve* [24].

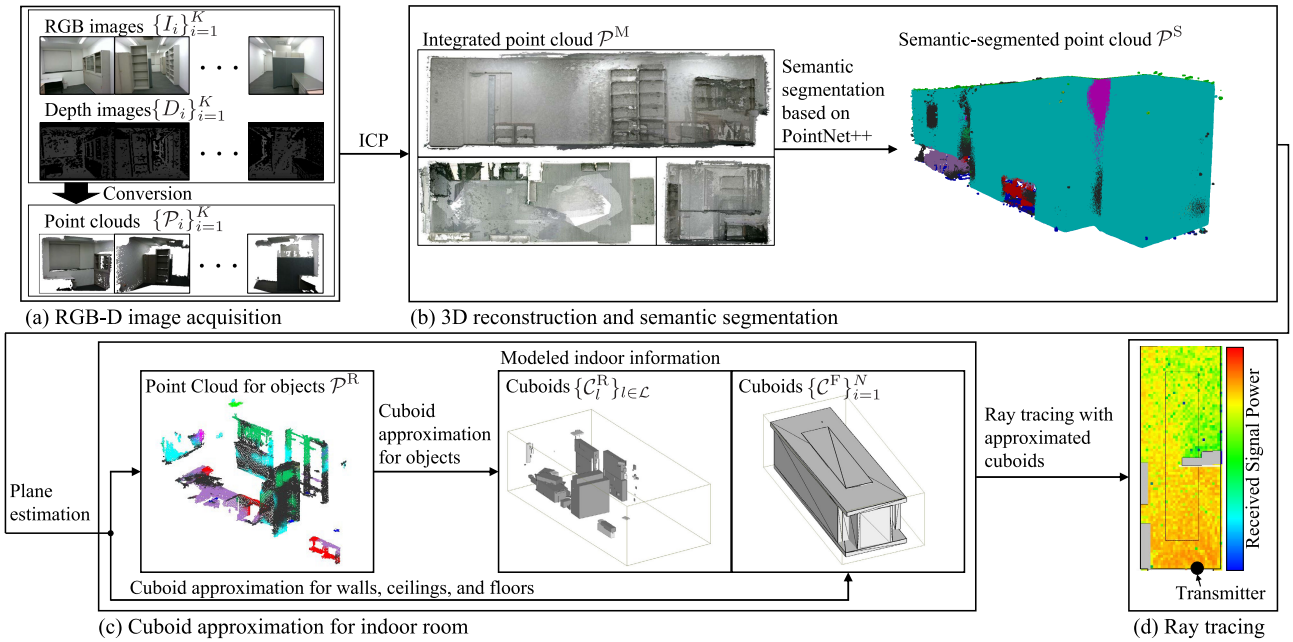

FIGURE 1. Processing flow of the proposed RGB-D sensor-assisted radio map construction framework.

compared various path loss models with actual measurements in an urban scenario. They revealed that their accuracy was limited even though the parameters in the models were tuned. Such experimental works have motivated the use of crowdsourcing-assisted REM construction. In crowdsourcing systems, nodes upload their sensing results with the measurement location and time to the server. The server then averages the instantaneous received signal power over small grids and compensates for the missing information based on spatial statistics. Reference [26] proposed a Kriging-based REM construction for outdoor scenarios; it was shown that Kriging could improve the accuracy of REM construction. Furthermore, various studies have evaluated the performance of such a method and expected it to be a promising technique for REM construction.

Several studies have been conducted on the application of radio maps to indoor applications [9], [27], [28], [29], [30], [31], [32], [33]. The authors in [29] applied a spatial statistics-based approach to indoor propagation modeling in 28 GHz. Their experimental results showed that the semivariogram outperforms the other statistics to describe shadowing statistics in path loss modeling in terms of the mean absolute error. In [9], the authors proposed a smartphone-aided radio map adaptation framework for indoor localization systems, while a study in [30] introduced a similar concept based on crowdsourcing. These works demonstrated that the crowdsourcing-based received signal power measurements could improve indoor localization accuracy. Additionally, [34] proposed a mechanism for radio map maintenance and updating in indoor scenarios. As with outdoor scenarios, such methods focus on estimating unknown received signal power values from limited measurements. However, their accuracy degrades due to the short shadowing correlation distance (centimeter to meter order [35], [36]). For example, an experimental study in [19] suggested that the accuracy enhancement by Kriging (i.e., an optimal spatial interpolation) is negligible compared to more straightforward approaches such as inverse distance weighting (IDW). Reference [33] introduced a deep Gaussian process for indoor localization. Experiments revealed that offline training with measurement signals from various access points (APs) could improve localization accuracy. However, such deep learning-based techniques tend to require a massive dataset. Unlike outdoor environments with a global positioning system (GPS), indoor environments are difficult to accurately measure the receiver location. From the viewpoint of tractability, it will be preferable to avoid obtaining the location information in sensing steps.

Radio maps can be constructed based on ray tracing in indoor and outdoor scenarios. However, the accuracy of ray tracing depends on the quality of the information about the structures and obstacles. Several countries actively develop 3D city models and publish them as vector data [37], [38], [39], which will help the ray-tracing-based radio map construction in outdoor scenarios. These models are classified into four levels according to the detail of the map (LOD: Level of Detail) and are being developed gradually. The models currently being converted to open data in various countries are LOD 1 or 2. Data at these levels store models that approximate outdoor information as a set of cuboids, and indoor information is out of focus and not currently applicable to indoor ray tracing.

The pros/cons of the radio map construction methods are summarized in Table 1. Among these methods, ray tracing is the preferred choice for achieving accurate indoor radio map construction if accurate structural information can be

obtained; however, it is difficult to obtain it freely. In this study for an accurate indoor radio map construction, we solve the drawback of indoor ray tracing simulation using RGB-D sensor-aided 3D reconstruction.

It is noteworthy that several researchers have focused on image sensor-aided millimeter-wave communication. In [40], a proactive received-power prediction method based on RGB-D images between wireless links was proposed. Influenced by this concept, the authors in [41] proposed a robust beamformer, assuming that the path-blockage probabilities are provided as prior information. However, the image between the links is not sufficient for bands ranging from several hundred MHz to GHz because both diffraction and reflections (i.e., effects of overall indoor objects) must be considered. To support the MHz-to-GHz bands, we propose to model the overall room/obstacle information as 3D data based on deep learning-aided post-processing.

III. PROPOSED FRAMEWORK

We define a radio map as a map that visualizes a transmitter's average power received per location. The received power is managed in each two-dimensional grid, which is several meters long on the side. The constructed map can be deployed on a transmitter/receiver or in the cloud, according to the application (e.g., WLAN resource optimization and localization).

The proposed framework is shown in Fig. 1 and Alg. 1. This framework constructs an indoor radio map based on the following steps: (a) image acquisition, (b) 3D reconstruction and semantic segmentation, (c) cuboid approximation for an indoor room, and (d) ray-tracing simulation. Each step is described in detail below:

A. RGB-D IMAGE ACQUISITION

We first capture K RGB and depth images, which are denoted as $\{I_i\}_{i=1}^K$ and $\{D_i\}_{i=1}^K$, respectively. These images are acquired over all areas in the target room using an RGB-D camera (Fig. 1(a)). Note that the depth images contain depth information as a pixel value and the pixel positions of the RGB and depth images correspond to the image plane dimension. These images are captured successively so that there are overlapping areas between the images of each viewpoint to successfully match the feature points between the images in the next step. The RGB and depth images, i.e., $\{I_i\}_{i=1}^K$ and $\{D_i\}_{i=1}^K$, are converted into colored point-cloud data, denoted as $\{\mathcal{P}_i\}_{i=1}^K$, for each view.

B. 3D RECONSTRUCTION AND SEMANTIC SEGMENTATION

Next, a semantic-segmented 3D point-cloud model is obtained for the target room from $\{\mathcal{P}_i\}_{i=1}^K$ (Fig. 1(b)). To integrate multiple point clouds into a 3D space, we use the iterative closest point (ICP) algorithm [42], [43], which is a registration algorithm for $\{\mathcal{P}_i\}_{i=1}^K$. This algorithm first finds the corresponding points between a pair of point-cloud data points and then repeatedly calculates the rotation and translation parameters, that is, $\boldsymbol{T}$, to minimize the distance metrics between the corresponding points. The objective function for the point clouds $\boldsymbol{p} \in \mathcal{P}$ and $\boldsymbol{q} \in \mathcal{Q}$ can be expressed as

$$\min_{\boldsymbol{T}} \sum_{(\boldsymbol{p},\boldsymbol{q})\in\mathcal{K}} \xi(\boldsymbol{p}, \boldsymbol{T}\boldsymbol{q}), \tag{1}$$

where $\xi(\cdot,\cdot)$ denotes the distance function of the points. In addition, $\mathcal{K}$ is a set of pairs of points corresponding to $\mathcal{P}$ and $\mathcal{Q}$. The pairs of corresponding points $(\boldsymbol{p}, \boldsymbol{q}) \in \mathcal{K}$ are obtained by mapping the nearest point $\boldsymbol{q}$ to each point $\boldsymbol{p} \in \mathcal{P}$ at an arbitrary iteration.

To obtain the 3D point-cloud model for the target room, we iterate the ICP algorithm on the point-cloud data of all viewpoints, that is, $\{\mathcal{P}_i\}_{i=1}^K$. The integrated 3D point-cloud model is expressed as $\mathcal{P}^M$. Subsequently, $\mathcal{P}^M$ is downsampled such that its density is lower than $d_{\min}[\mathrm{m}^{-3}]$ to reduce computational complexity.

Next, the integrated points are labeled according to the deep learning-aided semantic segmentation of the point-cloud data. A pre-trained PointNet++ [22] is used for semantic segmentation. This network classifies points into the following labels: $\mathcal{L} = \{$ceiling, floor, wall, beam, column, window, door, table, chair, sofa, bookcase, board, and clutter$\}$. We denote the semantic-segmented point-cloud data as $\mathcal{P}^S$.

C. CUBOID APPROXIMATION FOR INDOOR ROOM

In this step (Fig. 1(c)), the point-cloud data are approximated as a set of cuboids for ray-tracing simulations. To this end, $\mathcal{P}^S$ is divided into (i) a point cloud for walls, ceilings, and floors and (ii) another point cloud for other objects.

To extract the walls, ceilings, and floors from $\mathcal{P}^S$, we employ plane estimation [44]. This method finds a plane equation that minimizes the distance to a given point cloud $\mathcal{P}$:

$$\min_{a,b,c,d} \sum_{\boldsymbol{p}\in\mathcal{P}} \|\boldsymbol{p}\cdot(a,b,c)+d\|_2^2, \tag{2}$$

where a, b, c, and d are the parameters of the plane equation and $\|\cdot\|_2$ denotes the ℓ^2 norm operator. It is assumed that the number of walls, ceilings, and floors (as well as their directions) are known for plane estimation. We extract the point cloud corresponding to the estimated planes, which are denoted as $\{\mathcal{P}_i^F\}_{i=1}^N$ (N represents the number of planes). Subsequently, by finding the cube of the smallest volume that covers the point cloud, the cuboid corresponding to the point cloud for each plane, that is, $\{\mathcal{C}_i^F\}_{i=1}^N$, is obtained.

The remaining point-cloud data contain information about other objects such as desks, chairs, and displays. Thus, we approximate the remaining point cloud, that is, $\mathcal{P}^R \in \mathcal{P}^M \backslash \{\mathcal{P}_i^F\}_{i=1}^N$, as cuboids. In this process, point-cloud data are grouped for each piece of semantic information, that is, $\mathcal{P}_l^R (l \in \mathcal{L})$, via segmentation based on the Euclidean distance between points. If the Euclidean distance between the point clouds is less than ψ [m], these point clouds are assumed to be in the same object. The ground point-cloud data are denoted by $\{\mathcal{P}_{l,i}^R\}_{i=1}^{M_l}$, where M_l represents the number

Algorithm 1 Proposed Framework

Input: RGB and depth images, $\{I_i\}_{i=1}^{K}$ and $\{D_i\}_{i=1}^{K}$.

for all $I_i, D_i \leftarrow \{I_i\}_{i=1}^{K}$ and $\{D_i\}_{i=1}^{K}$ **do**
  Convert I_i and D_i into point cloud $\mathcal{P}_i$
end for
Create 3D model $\mathcal{P}^M$ from $\{\mathcal{P}_i\}_{i=1}^{K}$ by ICP
Obtain semantic segmented point cloud $\mathcal{P}^S$ from $\mathcal{P}^M$
Estimate planes $\{\mathcal{P}_i^F\}_{i=1}^{N}$ from $\mathcal{P}^S$
Approximate cuboids of walls, ceilings, and floors: $\{\mathcal{C}_i^F\}_{i=1}^{N}$, from $\{\mathcal{P}_i^F\}_{i=1}^{N}$
Obtain point cloud for rooms by $\mathcal{P}^R = \mathcal{P}^M \backslash \{\mathcal{P}_i^F\}_{i=1}^{N}$
for all $l \leftarrow$ semantic labels $\mathcal{L}$ **do**
  Segment objects, i.e., $\{\mathcal{P}_{l,i}^R\}_{i=1}^{M_l}$, according to Euclidean distance from $\mathcal{P}_l^R$
  for all $\mathcal{P}_{l,i}^R \leftarrow \{\mathcal{P}_{l,i}^R\}_{i=1}^{M_l}$ **do**
    Approximate cuboids of object $\mathcal{C}_{l,i}^R$ from $\mathcal{P}_{l,i}^R$
  end for
  $\mathcal{C}_l^R = \{\mathcal{C}_{l,i}^R\}_{i=1}^{M_l}$
end for
Environmental information $\mathcal{C} = \{\{\mathcal{C}^F\}_{i=1}^{N}, \{\mathcal{C}_l^R\}_{l\in\mathcal{L}}\}$
Estimate radio map using $\mathcal{C}$ via ray tracing

Output: Estimated radio map

of segmented objects on label l. We obtain the approximated cuboids $\mathcal{C}_l^R \in \{\mathcal{C}_{l,i}^R\}_{i=1}^{M_l}$ from $\{\mathcal{P}_{l,i}^R\}_{i=1}^{M_l}$ by finding the cube with the smallest volume that covers the points. These cuboids contain semantic information such as tables or chairs.

D. RAY TRACING WITH APPROXIMATED CUBOIDS

In this step (Fig. 1(d)), the ray-tracing simulation is performed using environmental information, i.e., $\mathcal{C} \in \{\{\mathcal{C}^F\}_{i=1}^{N}, \{\mathcal{C}_l^R\}_{l\in\mathcal{L}}\}$. The cuboids obtained in the previous step are labeled as their semantic information. Subsequently, according to the semantic information, we associate each cuboid with material information, such as thickness, roughness, conductivity, and permittivity. Furthermore, we initialize the ray-tracing model, such as the antenna type, antenna gain, antenna location, frequency, bandwidth, and transmission power. Finally, we run a ray-tracing calculation and obtain a radio map.

IV. MEASUREMENT CAMPAIGN

We conducted an indoor measurement campaign to evaluate the proposed framework using a WLAN system with a pair of transmitter/receiver devices.

A. MEASUREMENT AREAS

The experiment was conducted in two indoor rooms, an experimental room and an office room. The experimental room's photograph and top-view layout are shown in Fig. 2. The room size was 8.78 m wide, 3.44 m deep, and 2.5 m high. The transmitter is deployed on a central desk, as shown in Fig. 2(b). Red lines indicate the measurement points. The measurements were conducted at intervals of 0.1 m. In this

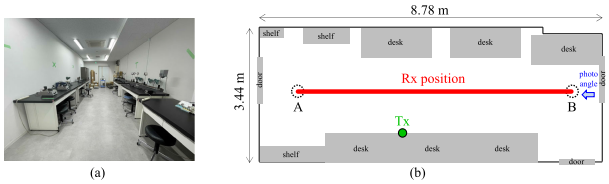

FIGURE 2. Experimental room: (a) overview, (b) top-view layout.

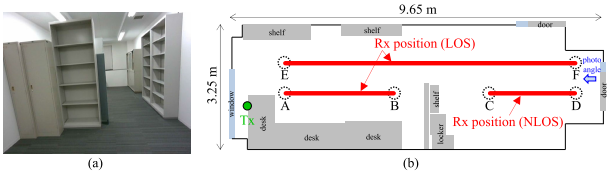

FIGURE 3. Office room: (a) overview, (b) top-view layout.

room, metallic desks were arranged along both sidewalls, and small experimental tools cluttered the desks. There were no blocking objects between the transmitter and receiver; thus, the setup was a line-of-sight (LOS) environment.

A photograph and a top-view layout of the office room are shown in Fig. 3. This room was 9.65 m wide, 3.25 m deep, and 2.50 m high. The transmitter is set beside the window, as shown in Fig. 3(b). Measurements were conducted along three lines (notated A–B, C–D, and E–F) in the figure. Two lockers and one shelf were placed at the center of the room, and these obstacles blocked the direct path between the transmitter and the receiver in the right-side region. Therefore, the right-side region (C–D) is a non-LOS (NLOS) environment, whereas the remaining region is a LOS environment. In contrast to the experimental room, the measurements in this room indicated shadowing effects.

B. MEASUREMENT CONFIGURATION

The measurement targets were the indoor received signal power values of over 2452 and 5180 MHz. For the transmitter, we used a laptop computer with Ubuntu 20.04 LTS and a USB WLAN device (Buffalo, WI-U2-433DHP). This device consists of a monopole antenna with a height of 0.93 m in the experimental room and 1.10 m in the office room. The transmission power was set as 20 dBm.

On the receiver side, we mounted another laptop computer with the same WLAN device on a two-stage cart with a height of 0.9 m, as shown in Fig. 4. The received signal power of the beacon signal of the target transmitter was measured ten times at 2-s intervals at one location using the iwconfig command.[2] Note that the iwconfig command can measure the received signal power value in the integer type in the dB domain.

An Intel RealSense D455 RGB-D camera[3] was used for RGB-D image acquisition. This camera can capture videos at 1280 × 720 pixels at a distance of 0.6-6.0 m. The camera was moved to capture images of the room at 30 frames per second (fps). The number of images K was 2296 and

[2]https://linux.die.net/man/8/iwconfig

[3]https://www.intel.com/content/www/us/en/products/sku/205847/intel-realsense-depth-camera-d455/specifications.html

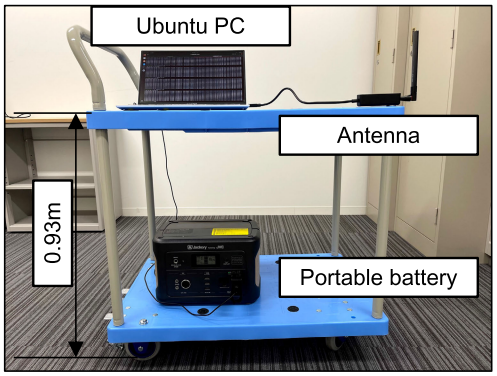

FIGURE 4. Measurement configuration.

TABLE 3. Parameters in ray-tracing simulations.

Frequency	5180 MHz, 2452 MHz
Bandwidth	16.6 MHz
Antenna type	Omnidirectional
Maximum antenna gain	1.76 dBi
Cable loss	0 dB
Maximum reflection number	6
Maximum diffraction number	2
Maximum penetration number	1
Ray-tracing algorithm	SBR
Ray spacing	0.25 deg.
Ray collection radius	several cm (depend on geometry)

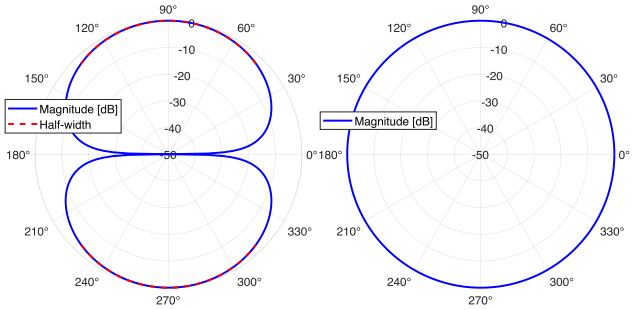

(a) Vertical (b) Horizontal

FIGURE 5. Antenna pattern of omnidirectional antenna used in ray-tracing simulation.

3248 for the experimental and office rooms, respectively. In the cuboid approximation, the density of the point cloud was set to a value below $d_{\min} = 0.025/\mathrm{m}^3$ via downsampling. The threshold of the segmentation-based Euclidean distance was set to $\psi = 0.025$ m.

C. COMPUTATION SETUP

The ray-tracing simulation was implemented using Wireless InSite.[4] This simulator uses a propagation model called X3D. This model is applicable to both outdoor and indoor environment simulation from 100 MHz to 100 GHz, which covers our experimental condition. This model is characterized by the shooting and bouncing ray (SBR) method [45] and the exact path calculation. Firstly, this model performs the rough ray launch method and finds the surfaces where reflection, penetration, and diffraction occur. Then, the imaging method is performed to find the paths that exactly reach the received point without a huge amount of path calculation. The electric field calculation is based on the reflection, penetration, and diffraction coefficients from the material-specific dielectric constant and conductivity. These coefficients are multiplied by the incident electric field when these incidents occur.

The key parameters in the ray tracing simulation are summarized in Table 3. This simulation assumed an omnidirectional antenna (Fig. 5) for both the transmitter and receiver (maximum gain 1.76 dBi) with a bandwidth of 16.6 MHz. Furthermore, the maximum number of reflections, diffractions, and penetrations were 6, 2, and 1, respectively. The points where the received power was calculated were placed linearly, as shown in Figs. 2 and 3. The interval between the received points in ray tracing was 0.01 m. In the proposed framework, the generated cuboid is labeled with its semantic information, and according to this information, the appropriate material is associated with the cuboid. The map information for ray tracing is generated using cuboids labeled with walls, ceilings, and floors, and we assume that these cuboids are treated as plaster. In contrast, objects are assumed to be made of metal. The reflection and penetration coefficients of the plaster material are shown in Fig. 6. In this figure, the attenuation of the parallel and perpendicular electric field is shown against the angle of incidence to the surface where reflection or penetration occurs. For metallic materials, no penetration occurs, and the material is assumed to reflect the ray without attenuation. The attenuation caused by diffraction has been determined according to references [46], [47]. The attenuation caused at the diffraction point is calculated based on Kouyoumijian's uniform geometrical theory of diffraction (UTD) [48]. If the angle of incidence ray is φ' and the angle of diffraction is φ (see Fig. 7), the diffraction coefficient is calculated as a superposition of the functions $D^+(\varphi \pm \varphi')$ and $D^-(\varphi \pm \varphi')$ (see Appendix). Fig. 7 shows the values of the functions $D^+(\varphi \pm \varphi')$ and $D^-(\varphi \pm \varphi')$ for the diffraction angle when the incident angle φ' is 45 degree. As can be seen from the figure, diffracted ray has peak amplitudes in the incident and reflected ray directions.

The propagation model used in the X3D model is the classical one, based on UTD proposed by Kouyoumijian [48], and more generic or accurate models have been proposed in recent years. For example, ray-tracing models in the THz band have been investigated [49], and models that use deep learning in combination with ray tracing have been studied extensively [50], [51]. Although we assume ray tracing based on [48] in this paper, the function of 3D reconstruction is separated from ray tracing. Therefore, the approach proposed in this paper can be used in combination with the latest ray-tracing models, which is one of the future considerations.

V. EVALUATION RESULTS

A. COMPARISON OF MEASURED AND SIMULATED PERFORMANCES

Fig. 8 presents comparisons between the received-power measurement and the ray-tracing calculation for four scenar-

[4]https://www.remcom.com/wireless-insite-em-propagation-software

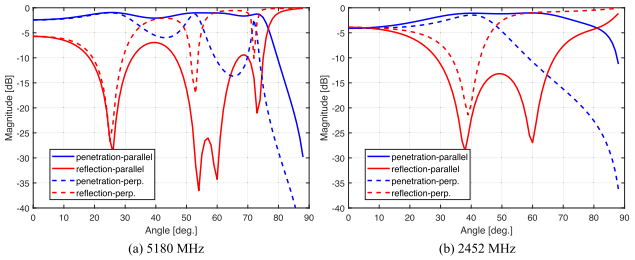

(a) 5180 MHz (b) 2452 MHz

FIGURE 6. Reflection and penetration coefficients.

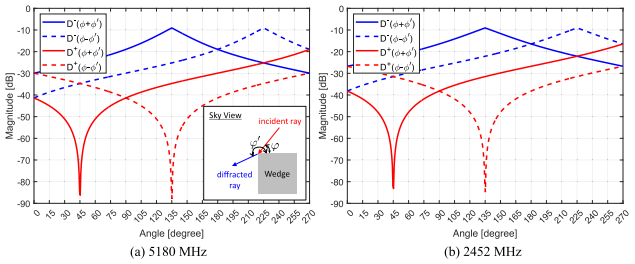

(a) 5180 MHz (b) 2452 MHz

FIGURE 7. $D^{\pm}(\varphi \pm \varphi')$ value used in diffraction calculation.

ios (experimental room with 5180 MHz, office room with 5180 MHz, experimental room with 2452 MHz, and office room with 2452 MHz). The performance of the proposed framework in the LOS environment (experimental room) is shown in Figs. 8 (a) and (b). The received signal power was obtained ten times at each measurement position. Since the iwconfig command outputs the received power with a granularity of 1 dB, the scatters in Fig. 8 overlap at each position partially. Although the overall received power levels at 5180 and 2452 MHz were different, the proposed method captured the shape of the received-power variation against the distance in both cases.

The results for the LOS/NLOS mixed environment (office room) are shown in Figs. 8(c)-(f). Metallic obstacles were installed in the central region of the office room, and the region between C and D in Figs. 8 (c) and (d) was in the NLOS environment. The proposed method accurately captured the step-like received-power fluctuations, as observed in the NLOS region. The proposed framework can accurately estimate site-specific characteristics by using RGB-D images.

B. ACCURACY ANALYSIS

There have been several discussions on radio-map construction based on RSSI crowdsensing [1]. In this method, receivers provide feedback on the RSSI quality, their sensing location, time, and channel, to a centralized server. The server then constructs the radio map while interpolating the missing areal information. One may question whether image or RSSI sensing is better for indoor radio map construction.

To discuss this question, we compared the performance of RSSI sensing using Kriging, an optimal spatial interpolation approach [19]. Kriging interpolates the received signal power at coordinate $\boldsymbol{x}_0$ from the training dataset [52], [53]. Let us define the dataset for Kriging as

$$\mathcal{D} = \{[\boldsymbol{x}_1, P(\boldsymbol{x}_1)], [\boldsymbol{x}_2, P(\boldsymbol{x}_2)], \cdots, [\boldsymbol{x}_n, P(\boldsymbol{x}_n)]\}, \quad (3)$$

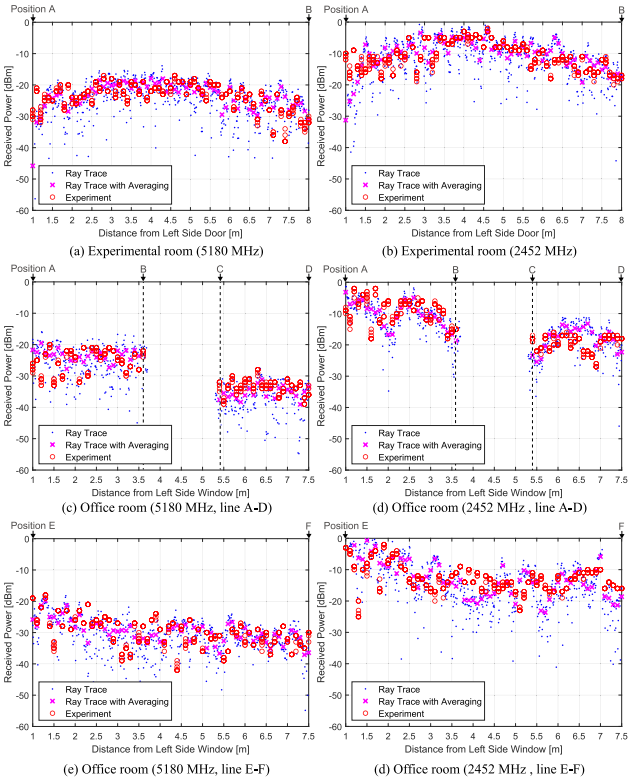

(a) Experimental room (5180 MHz) (b) Experimental room (2452 MHz)
(c) Office room (5180 MHz, line A-D) (d) Office room (2452 MHz , line A-D)
(e) Office room (5180 MHz, line E-F) (d) Office room (2452 MHz , line E-F)

FIGURE 8. Measurement and estimated received-power values. Magenta cross-mark scatter shows the averaged received power with two wavelength regions centered at each measurement location.

where n denotes the number of training data points, $\boldsymbol{x}_i$ denotes the i-th measurement location, and $P(\boldsymbol{x}_i)$ denotes the received power at $\boldsymbol{x}_i$. In this context, the task of Kriging involves accurately estimating the received power at an unmeasured location $\boldsymbol{x}_0$ from $\mathcal{D}$.

We assume ordinary Kriging in this task; this method can construct the radio map without the transmitter's information, such as transmission power and location. The received signal power at coordinate $\boldsymbol{x}$ can be modeled as

$$P(\boldsymbol{x}) = P_{\mathrm{Tx}} - 10\eta \log_{10} \|\boldsymbol{x}_{\mathrm{Tx}} - \boldsymbol{x}\|_2 + W(\boldsymbol{x}), \quad (4)$$

where P_{Tx} represents the transmission power, η is the path loss index, $\boldsymbol{x}_{\mathrm{Tx}}$ represents the transmitter location, and $W(\boldsymbol{x})$ represents spatially correlated shadowing. This method estimates $P(\boldsymbol{x})$ based on the weighted averaging formulated as $\hat{P}(\boldsymbol{x}_0) = \sum_{i=1}^{n} \omega_i P(\boldsymbol{x}_i)$, where ω_i is the weighting factor for the i-th measurement. Ordinary Kriging optimizes the weighting factors such that the error variance is minimized under a constraint for unbiased estimation, which is formulated as

$$\min_{\{\omega_1, \omega_2, \cdots, \omega_n\}} \mathrm{Var}\left[\hat{P}(\boldsymbol{x}_0) - P(\boldsymbol{x}_0)\right]$$
$$\text{subject to } \sum_{i=1}^{n} \omega_i = 1. \quad (5)$$

For performance evaluation, we first calculated the radio map obtained using the proposed method for each scenario at

1-cm intervals when the parameter ψ was set to 0.025. In this evaluation, 30 test data points were randomly selected from the estimation results, and the estimation error was evaluated for each location. This process was repeated 1000 times, and the root-mean-square error (RMSE) was evaluated using the following equation:

$$\mathrm{RMSE} = \sqrt{\frac{1}{n_{\mathrm{test}}} \sum_{j=1}^{n_{\mathrm{test}}} \left(\hat{P}(\boldsymbol{x}_{\mathrm{test},j}) - P(\boldsymbol{x}_{\mathrm{test},j}) \right)} \ [\mathrm{dB}], \quad (6)$$

where $n_{\mathrm{test}} (= 30\,[\mathrm{points}] \times 1000\,[\mathrm{trials}])$ is the number of test data and $\boldsymbol{x}_{\mathrm{test},j}$ is the j-th test location. The accuracy of the RSSI-based method depends on the amount of sensing data. For the RSSI-based method, we evaluated by randomly acquiring N_{train} training data, evaluating the estimation accuracy for test data from 30 randomly selected instantaneous samples without overlap, and repeating the above process 1000 times with different numbers of training data. This study aims to predict the effects of path loss and shadowing for radio map construction. To sufficiently remove the multi-path fading, the ray-tracing simulation results with the granularity 0.01 m were averaged over two wavelengths centered on each measurement position in advance.

Fig. 9 shows the RMSE performance at (a) 5180 MHz and (b) 2452 MHz. The RMSE of Kriging decreased with an increase in the amount of data. However, the proposed method was better than the Kriging-based method in various conditions, specifically in small measurement sample regions. In indoor situations, we can use ray tracing with the proposed image-based method to construct radio maps accurately. The RSSI-based method requires the measurement of absolute receiver coordinates, making it crucial to implement an accurate positioning method, such as Wi-Fi round-trip time.[5] In contrast, the proposed method acquires 3D point clouds in relative coordinates based on consistency between images. This feature implies that the proposed method is advantageous regarding the sensing cost. Therefore, this feature can reduce the evaluation cost in the pre-evaluation task, e.g., access point (AP) deployment optimization.

C. EFFECTS OF EXPERIMENTAL PARAMETERS

If parameter ψ increases, the number of point clouds assigned to a single cuboid tends to increase; consequently, only a few large cuboids are generated. In contrast, a small ψ may result in many small cuboids. Because the accuracy of ray tracing is significantly affected by the size and number of cuboids, we evaluated the impact of ψ on the estimation accuracy. Table 4 shows the effects of ψ on RMSE performances.

For all settings, decreasing ψ (i.e., increasing the number of cuboids) tends to improve the estimation accuracy. Several settings failed to perform ray tracing (we denoted these results as *NaN*) because the transmitter or received points were located in a cuboid. Although the smaller ψ tends

[5]https://developer.android.com/guide/topics/connectivity/wifi-rtt

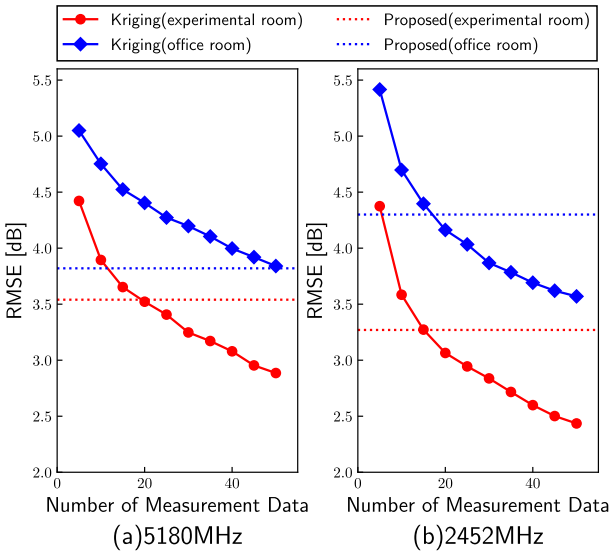

FIGURE 9. RMSE performance.

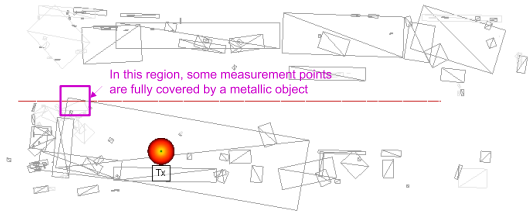

FIGURE 10. Object location and received position for $\psi = 0.05$ (experimental room).

to improve the accuracy, *NaN* happened with $\psi = 0.05$. This is because metal objects fully covered a few receiver points, and no path reached these points. The ray-tracing result could not be obtained in such an area; thus, the RMSE calculation failed (see Fig. 10). For such failed points, we indicated 1) the RMSE when the invalid ray-tracing results are excluded, and 2) the percentage of successfully achieved ray-tracing results. For example, received signal power values at 36.5% evaluation points were successfully computed at the office scenario with 2452MHz and $\psi = 0.5\,[\mathrm{m}]$. Even in such cases, the received power could be computed for most receiver points with an accurate approximation of the experimental data. This phenomenon can occur with any threshold value, depending on the relationship between the cuboids and the receiver points. Whether the transmitter/receiver is covered can be visually confirmed from the layouts of the approximated cuboids, and we can avoid it by taking a smaller ψ with better accuracy. Thus, this phenomenon will be acceptable in practical propagation simulations.

Fig. 11 illustrates 3D reconstruction examples with $\psi = 0.500, 0.100, 0.050$, and $0.025\,[\mathrm{m}]$. Increasing ψ frequently generates large objects. If an object covers the transmitter, no receiver can measure the signal power values because all the transmitted rays are closed in the metallic object. This phenomenon can also occur when ψ is small (e.g.,

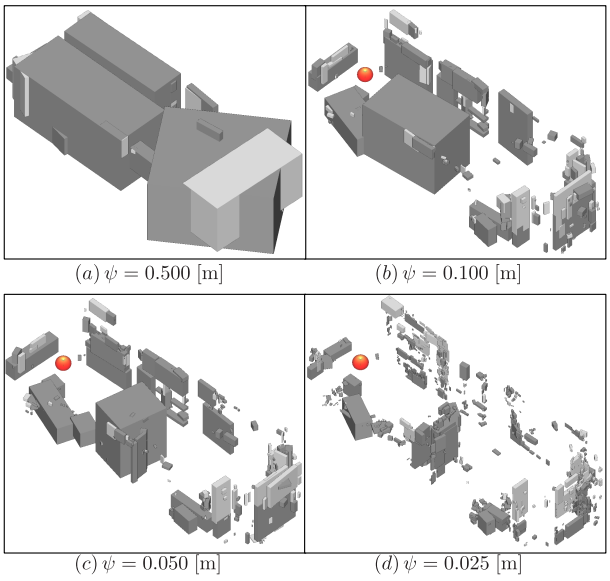

FIGURE 11. 3D reconstruction examples in office room.

$\psi = 0.05$ and 5180 MHz in an experimental room). Fortunately, the possibility of ray tracing can be confirmed when the transmitter/receiver is plotted on a 3D reconstructed map. In practice, taking ψ as small as 0.025 m and visually confirming the 3D reconstruction results before the ray-tracing simulation is preferable.

We verified the approximation accuracy of cuboids as a benchmark [54]. We define a metric for the approximation accuracy as the mean absolute error (MAE) of the Euclidean distance between the point cloud contained by the cuboid contains and the nearest surface of the cuboid. The MAE for a cuboid $\mathcal{C}$ and its corresponding point cloud $\mathcal{P}$ is defined as

$$\mathrm{MAE} = \sum_{\boldsymbol{p}\in\mathcal{P}} \min_{\{a,b,c,d\}\in\Omega(\mathcal{C})} \left| \frac{\boldsymbol{p}\cdot(a,b,c)+d}{\sqrt{a^2+b^2+c^2}} \right|, \qquad (7)$$

where $\Omega(\mathcal{C})$ is an operator that obtains a set of parameters (a, b, c, and d) of the plane equation for cuboid surfaces of cuboid $\mathcal{C}$.

Fig. 12 shows the box plot for the accuracy of the cuboid approximation. The MAE performance was improved as the parameter ψ became smaller. The accuracy of walls, floor, and ceiling was almost constant without depending on ψ. These results indicate that the proposed method can obtain good accuracy of the cuboid approximation as parameter ψ becomes smaller.

We show the effects of fps on the RMSE in Table 5. The influence of fps was evaluated by extracting images from videos captured at 30 fps at equal intervals. Further, as with Table 4, we indicated RMSEs when the invalid ray-tracing results are excluded and the percentage of successfully achieved ray-tracing results. Table 5 shows that the ray-tracing simulation was stable at 15 fps or higher for all settings. However, when the fps is small, ray tracing cannot be performed in the low-fps region. This

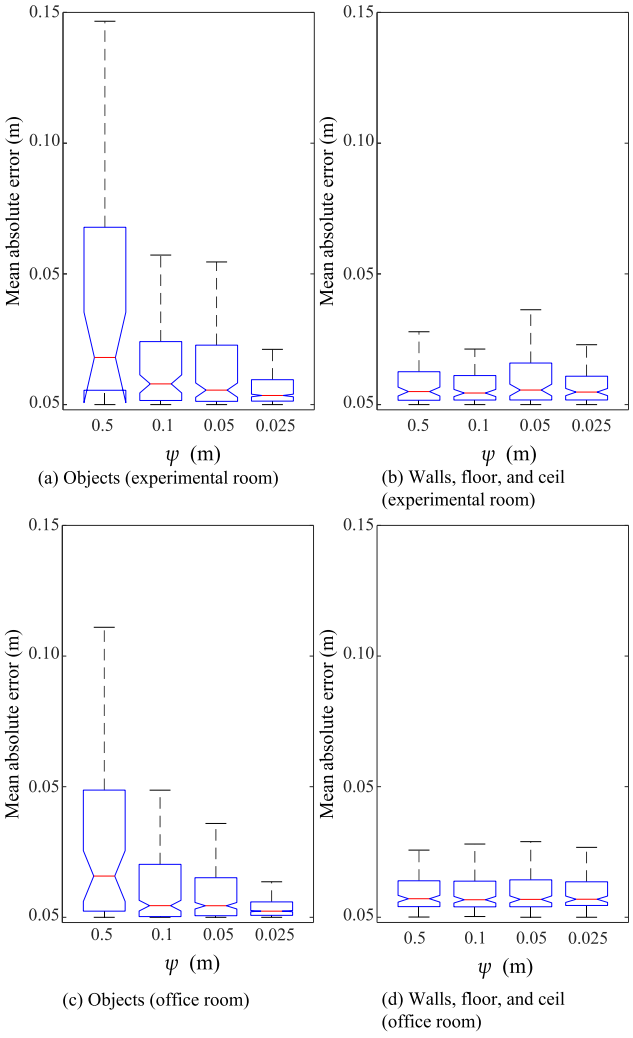

FIGURE 12. MAE performances for the cuboid approximation. The boxplots depict the lower and upper quartiles, and the red line represents the median values. The top and bottom ends of the whiskers represent the maximal and minimal values of nonoutliers, respectively. The top and bottom edges of the notch region correspond to the 95% confidence interval of these median values.

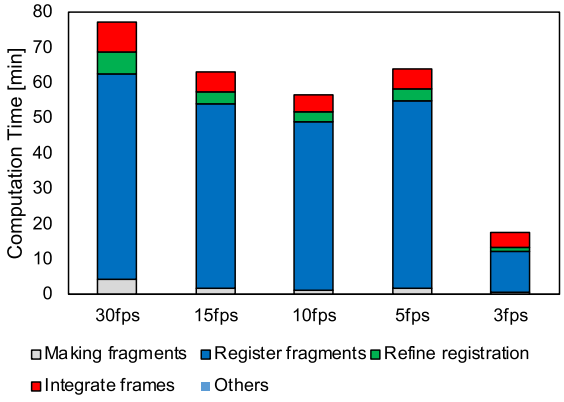

FIGURE 13. Effect of fps on the computation time at the office room.

is because the 3D reconstruction using the ICP algorithm (Fig. 1(b)) is not accurate when fps is small. If the fps is small, the amount of frame-to-frame motion increases.

TABLE 4. Effect of ψ on RMSE performances. We highlighted the best performance in each set by **bold**. Element with "NaN (*A*, *B*%)" indicates that the RMSE was not available since received signal power values could not be computed in part: *A* is the RMSE [dB] when the invalid ray-tracing results are excluded, and *B*% is the percentage of successfully achieved results by the ray tracing.

	Experimental Room		Office Room	
Threshold[m]	2452 MHz	5180 MHz	2452 MHz	5180 MHz
0.5	28.8	NaN (14.0, 74.6%)	NaN (14.5, 36.5%)	NaN (7.49, 34.8%)
0.1	3.46	3.74	5.69	18.6
0.05	6.36	NaN (6.34, 98.6%)	4.97	6.84
0.025	**3.27**	**3.54**	**4.30**	**3.82**

TABLE 5. Effect of fps on RMSE performances. How to read each element is as with Table 4.

	Experimental Room		Office Room	
fps	2452 MHz	5180 MHz	2452 MHz	5180 MHz
3	7.14	11.2	NaN (5.97, 99.13%)	6.64
5	15.2	NaN (16.6, 98.59%)	NaN (14.2, 96.5%)	NaN (9.28, 99.13%)
10	**3.13**	3.65	5.03	NaN (10.3, 99.13%)
15	3.19	**3.40**	7.38	3.96
30	3.27	3.54	**4.30**	**3.82**

TABLE 6. Effects of fps on the size of point clouds (office room).

fps	Number of Points
3	46315990
5	52535424
10	43705494
15	15978665
30	15978665

In such cases, it is difficult to estimate the rotation and translation parameters in the ICP algorithm; thus, the 3D reconstruction is inaccurate. Therefore, the accuracy of the cuboid approximation deteriorates in small fps cases. Although the accuracy at 30 fps is not necessarily the best, the difference between the best value and RMSE at 30 fps is sufficiently small. Table 6 summarizes the effects of the fps on the number of points. It is observed that the number of point clouds has an increasing trend with lower fps. This is primarily because the parameters cannot be estimated correctly, as described above, and the corresponding point clouds between frames do not match and merge.

Finally, we show the effects of fps on the computation time in Fig. 13. This figure shows the computation time required for the 3D reconstruction (Fig. 1(b)), which is dominant in the proposed method. We implemented the simulation program with Python 3.8.11 and ran it on a computer with Ubuntu 20.04.4 LTS. This computer was equipped with an Intel Core i9-10980XE (18 cores, 36 threads with 4.80 GHz clock at the maximum) and DDR4 128 GB memory. The case with 30 fps required the longest computation time (approximately 80 min), whereas the shortest time was realized at three fps (approximately 20 min). The computation time tends to be smaller for more petite fps, but the accuracy is degraded in the lower fps case described above; thus, there is a trade-off relationship. To summarize the influence of fps in practice, because reducing the fps of an image captured at a high fps requires only equally spaced image sampling, it is preferable to take images at 30 fps and adjust the fps during 3D reconstruction according to the required accuracy of ray tracing.

VI. CONCLUSION

This study proposed a new framework for indoor radio map construction based on image sensing, 3D reconstruction, deep learning, and ray tracing. The proposed method models indoor information from RGB-D images as a set of cuboids. Both room materials and obstacles can be converted into vector data, and thus, we can realize a ray-tracing simulation with precise indoor information.

Based on WLAN systems, we performed indoor experiments for two scenarios, over 5180 and 2452 MHz. The experimental results indicated that the proposed method achieved better accuracy than the RSSI sensing-based method for various scenarios. The image-based method can construct indoor radio maps via ray-tracing simulations once the images are acquired. This feature can reduce the evaluation cost of a pre-evaluation task, for example, AP deployment optimization.

APPENDIX

A. CALCULATION OF DIFFRACTION COEFFICIENT

In general, the diffraction coefficient is calculated in the edge-fixed coordinate system [55]. We define the unit vector $\boldsymbol{l}$, which is parallel to the wedge. The propagation vector of the incident ray is also defined as $\boldsymbol{k}'$ Then, the following unit vectors are obtained as:

$$\boldsymbol{\phi}' = \frac{-\boldsymbol{l} \times \boldsymbol{k}'}{|\boldsymbol{l} \times \boldsymbol{k}'|}, \tag{8}$$

$$\boldsymbol{\beta}' = \boldsymbol{\phi}' \times \boldsymbol{k}'. \tag{9}$$

The incident field $\boldsymbol{E}^i$ is decomposed into $\boldsymbol{\phi}'$ and $\boldsymbol{\beta}'$ components as $E^i_{\boldsymbol{\phi}'} = \boldsymbol{E}^i \cdot \boldsymbol{\phi}'$ and $E^i_{\boldsymbol{\beta}'} = \boldsymbol{E}^i \cdot \boldsymbol{\beta}'$, respectively. The $\boldsymbol{\phi}'$ and $\boldsymbol{\beta}'$ components of the diffracted field is given by:

$$\begin{bmatrix} E^d_{\boldsymbol{\beta}} \\ E^d_{\boldsymbol{\phi}} \end{bmatrix} = \begin{bmatrix} D_{ss} & D_{sh} \\ D_{hs} & D_{hh} \end{bmatrix} \begin{bmatrix} E^i_{\boldsymbol{\beta}'} \\ E^i_{\boldsymbol{\phi}'} \end{bmatrix} \cdot \sqrt{\frac{r_{TD} \cdot r_{DR}}{r_{TD} + r_{DR}}} \frac{e^{-j\beta r_{DR}}}{r_{DR}} \tag{10}$$

where r_{TD} is the distance between the source of the incident ray and the diffraction point, and r_{TD} is the distance between

the diffraction point and the receiver location. The values D_{ss}, D_{sh}, D_{hs}, and D_{hh} are known as diffraction coefficient and can be calculated as:

$$\begin{aligned} D_{ss} &= D^{+}\left(\varphi-\varphi'\right)+D^{-}\left(\varphi-\varphi'\right) \\ &\quad-\left(R_{\parallel}^{0}\cos^{2}\alpha_{1}-R_{\perp}^{0}\sin^{2}\alpha_{1}\right)D^{-}\left(\varphi+\varphi'\right) \\ &\quad-\left(R_{\parallel}^{\rho}\cos^{2}\alpha_{2}-R_{\perp}^{\rho}\sin^{2}\alpha_{2}\right)D^{+}\left(\varphi+\varphi'\right), \end{aligned} \tag{11}$$

$$\begin{aligned} D_{hh} &= D^{+}\left(\varphi-\varphi'\right)+D^{-}\left(\varphi-\varphi'\right) \\ &\quad+\left(R_{\parallel}^{0}\sin^{2}\alpha_{1}-R_{\perp}^{0}\cos^{2}\alpha_{1}\right)D^{-}\left(\varphi+\varphi'\right) \\ &\quad+\left(R_{\parallel}^{\rho}\sin^{2}\alpha_{2}-R_{\perp}^{\rho}\cos^{2}\alpha_{2}\right)D^{+}\left(\varphi+\varphi'\right), \end{aligned} \tag{12}$$

$$\begin{aligned} D_{sh} &= -\left(R_{\parallel}^{0}+R_{\perp}^{0}\right)\cos\alpha_{1}\sin\alpha_{1}D^{-}\left(\varphi+\varphi'\right) \\ &\quad-\left(R_{\parallel}^{\rho}+R_{\perp}^{\rho}\right)\cos\alpha_{2}\sin\alpha_{2}D^{+}\left(\varphi+\varphi'\right), \end{aligned} \tag{13}$$

$$\begin{aligned} D_{hs} &= \left(R_{\parallel}^{0}+R_{\perp}^{0}\right)\cos\alpha_{1}\sin\alpha_{1}D^{-}\left(\varphi+\varphi'\right) \\ &\quad+\left(R_{\parallel}^{\rho}+R_{\perp}^{\rho}\right)\cos\alpha_{2}\sin\alpha_{2}D^{+}\left(\varphi+\varphi'\right). \end{aligned} \tag{14}$$

The 0 and ρ superscripts represent the two sides of the wedge as in [46] and [47]; φ and φ' are the diffraction and incidence angles as shown in Fig. 7(a). The angles α_1 and α_2 are determined from $\sin\alpha_1 = \boldsymbol{e}_{\parallel}^{0}\cdot\boldsymbol{\phi}'$ and $\sin\alpha_2 = \boldsymbol{e}_{\parallel}^{\rho}\cdot\boldsymbol{\phi}'$, where the unit vectors $\boldsymbol{e}_{\parallel}^{0}$ and $\boldsymbol{e}_{\parallel}^{\rho}$ are the ray-fixed vectors parallel to the plane of incidence. The functions $D^{\pm}\left(\varphi\pm\varphi'\right)$ are given by:

$$\begin{aligned} D^{\pm}\left(\varphi\pm\varphi'\right) &= \frac{-e^{-j\pi/4}}{2\rho\sqrt{2\pi k}}\cot\left(\frac{\pi\pm\left(\varphi\pm\varphi'\right)}{2\rho}\right) \\ &\quad\cdot F\left(kLa^{\pm}\left(\varphi\pm\varphi'\right)\right) \end{aligned} \tag{15}$$

where $F\left(kLa^{\pm}\left(\varphi\pm\varphi'\right)\right)$ is the Fresnel integral, defined in several references [46], [48].

ACKNOWLEDGMENT

(The authors contributed equally to this work.)

REFERENCES

[1] S. Bi, J. Lyu, Z. Ding, and R. Zhang, "Engineering radio maps for wireless resource management," *IEEE Wireless Commun.*, vol. 26, no. 2, pp. 133–141, Apr. 2019.

[2] Y. Zhao, L. Morales, J. Gaeddert, K. K. Bae, J.-S. Um, and J. H. Reed, "Applying radio environment maps to cognitive wireless regional area networks," in *Proc. 2nd IEEE Int. Symp. New Frontiers Dyn. Spectr. Access Netw.*, Apr. 2007, pp. 115–118.

[3] R. Murty, R. Chandra, T. Moscibroda, and P. Bahl, "SenseLess: A database-driven white spaces network," in *Proc. IEEE Int. Symp. Dyn. Spectr. Access Netw. (DySPAN)*, May 2011, pp. 10–21.

[4] H. R. Karimi, "Geolocation databases for white space devices in the UHF TV bands: Specification of maximum permitted emission levels," in *Proc. IEEE Int. Symp. Dyn. Spectr. Access Netw. (DySPAN)*, May 2011, pp. 443–454.

[5] K. Sato, K. Inage, and T. Fujii, "Modeling the Kriging-aided spatial spectrum sharing over log-normal channels," *IEEE Wireless Commun. Lett.*, vol. 8, no. 3, pp. 749–752, Jun. 2019.

[6] H. Gacanin and A. Ligata, "Wi-Fi self-organizing networks: Challenges and use cases," *IEEE Commun. Mag.*, vol. 55, no. 7, pp. 158–164, Jul. 2017.

[7] J. Perez-Romero, A. Zalonis, L. Boukhatem, A. Kliks, K. Koutlia, N. Dimitriou, and R. Kurda, "On the use of radio environment maps for interference management in heterogeneous networks," *IEEE Commun. Mag.*, vol. 53, no. 8, pp. 184–191, Aug. 2015.

[8] X. Mo, Y. Huang, and J. Xu, "Radio-map-based robust positioning optimization for UAV-enabled wireless power transfer," *IEEE Wireless Commun. Lett.*, vol. 9, no. 2, pp. 179–183, Feb. 2020.

[9] C. S. Wu, Z. Yang, and C. Xiao, "Automatic radio map adaptation for indoor localization using smartphones," *IEEE Trans. Mobile Comput.*, vol. 17, no. 3, pp. 517–528, Mar. 2018.

[10] Q. Jiang, Y. Ma, K. Liu, and Z. Dou, "A probabilistic radio map construction scheme for crowdsourcing-based fingerprinting localization," *IEEE Sensors J.*, vol. 16, no. 10, pp. 3764–3774, Feb. 2016.

[11] M. M. Atia, A. Noureldin, and M. J. Korenberg, "Dynamic online-calibrated radio maps for indoor positioning in wireless local area networks," *IEEE Trans. Mobile Comput.*, vol. 12, no. 9, pp. 1774–1787, Sep. 2013.

[12] Y. Tao and L. Zhao, "A novel system for WiFi radio map automatic adaptation and indoor positioning," *IEEE Trans. Veh. Technol.*, vol. 67, no. 11, pp. 10683–10692, Nov. 2018.

[13] H. Zou, M. Jin, H. Jiang, L. Xie, and C. J. Spanos, "WinIPS: WiFi-based non-intrusive indoor positioning system with online radio map construction and adaptation," *IEEE Trans. Wireless Commun.*, vol. 16, no. 12, pp. 8118–8130, Dec. 2017.

[14] S. Sorour, Y. Lostanlen, S. Valaee, and K. Majeed, "Joint indoor localization and radio map construction with limited deployment load," *IEEE Trans. Mobile Comput.*, vol. 14, no. 5, pp. 1031–1043, May 2015.

[15] Q. D. Vo and P. De, "A survey of fingerprint-based outdoor localization," *IEEE Commun. Surveys Tuts.*, vol. 18, no. 1, pp. 491–506, 1st Quart., 2015.

[16] R. Ayyalasomayajula, A. Arun, C. Wu, S. Sharma, A. R. Sethi, D. Vasisht, and D. Bharadia, "Deep learning based wireless localization for indoor navigation," in *Proc. 26th Annu. Int. Conf. Mobile Comput. Netw.*, Apr. 2020, pp. 1–14.

[17] M. Wellens, J. Riihijärvi, and P. Mähönen, "Spatial statistics and models of spectrum use," *Comput. Commun.*, vol. 32, no. 18, pp. 1998–2011, Dec. 2009. [Online]. Available: https://www.sciencedirect.com/science/article/pii/S0140366409002242

[18] S. Szyszkowicz, H. Yanikomeroglu, and J. Thompson, "On the feasibility of wireless shadowing correlation models," *IEEE Trans. Veh. Technol.*, vol. 59, no. 9, pp. 4222–4236, Nov. 2010.

[19] Z. El-friakh, A. M. Voicu, S. Shabani, L. Simic, and P. Mahonen, "Crowdsourced indoor Wi-Fi REMs: Does the spatial interpolation method matter?" in *Proc. IEEE Int. Symp. Dyn. Spectr. Access Netw. (DySPAN)*, Oct. 2018, pp. 1–10.

[20] C. Phillips, D. Sicker, and D. Grunwald, "A survey of wireless path loss prediction and coverage mapping methods," *IEEE Commun. Surveys Tuts.*, vol. 15, no. 1, pp. 255–270, 1st Quart., 2013.

[21] A. Tayebi, J. G. Perez, F. M. S. D. A. Herrero, and O. Gutierrez, "The application of ray-tracing to mobile localization using the direction of arrival and received signal strength in multipath indoor environments," *Prog. Electromagn. Res.*, vol. 91, pp. 1–15, 2009.

[22] C. R. Qi, L. Yi, H. Su, and L. J. Guibas, "PointNet++: Deep hierarchical feature learning on point sets in a metric space," in *Proc. NeurIPS*, 2017, pp. 1–10.

[23] Y. Zhao, J. Gaeddert, L. Morales, K. Bae, J.-S. Um, and J. H. Reed, "Development of radio environment map enabled case- and knowledge-based learning algorithms for IEEE 802.22 WRAN cognitive engines," in *Proc. 2nd Int. Conf. Cognit. Radio Oriented Wireless Netw. Commun.*, Aug. 2007, pp. 44–49.

[24] S. Bhattarai, J.-M. J. Park, B. Gao, K. Bian, and W. Lehr, "An overview of dynamic spectrum sharing: Ongoing initiatives, challenges, and a roadmap for future research," *IEEE Trans. Cogn. Commun. Netw.*, vol. 2, no. 2, pp. 110–128, Jun. 2016.

[25] C. Phillips, D. Sicker, and D. Grunwald, "Bounding the error of path loss models," in *Proc. IEEE Int. Symp. Dyn. Spectr. Access Netw. (DySPAN)*, May 2011, pp. 71–82.

[26] C. Phillips, M. Ton, D. Sicker, and D. Grunwald, "Practical radio environment mapping with geostatistics," in *Proc. IEEE Int. Symp. Dyn. Spectr. Access Netw.*, Oct. 2012, pp. 422–433.

[27] S. H. Jung, B.-C. Moon, and D. Han, "Performance evaluation of radio map construction methods for Wi-Fi positioning systems," *IEEE Trans. Intell. Transp. Syst.*, vol. 18, no. 4, pp. 880–889, Apr. 2017.

[28] M. E. Diago-Mosquera, A. Aragón-Zavala, and G. Castañón, "Bringing it indoors: A review of narrowband radio propagation modeling for enclosed spaces," *IEEE Access*, vol. 8, pp. 103875–103899, 2020.
[29] M. Diago-Mosquera, A. Aragon-Zavala, L. Azpilicueta, R. Shubair, and F. Falcone, "A 3-D indoor analysis of path loss modeling using Kriging techniques," *IEEE Antennas Wireless Propag. Lett.*, vol. 21, no. 6, pp. 1218–1222, Jun. 2022.
[30] X. Du, X. Liao, M. Liu, and Z. Gao, "CRCLoc: A crowdsourcing-based radio map construction method for WiFi fingerprinting localization," *IEEE Internet Things J.*, vol. 9, no. 14, pp. 12364–12377, Jul. 2022.
[31] Y. Ye and B. Wang, "RMapCS: Radio map construction from crowdsourced samples for indoor localization," *IEEE Access*, vol. 6, pp. 24224–24238, 2018.
[32] H. Zou, C.-L. Chen, M. Li, J. Yang, Y. Zhou, L. Xie, and C. J. Spanos, "Adversarial learning-enabled automatic WiFi indoor radio map construction and adaptation with mobile robot," *IEEE Internet Things J.*, vol. 7, no. 8, pp. 6946–6954, Aug. 2020.
[33] X. Wang, X. Wang, S. Mao, J. Zhang, S. C. G. Periaswamy, and J. Patton, "Indoor radio map construction and localization with deep Gaussian processes," *IEEE Internet Things J.*, vol. 7, no. 11, pp. 11238–11249, Nov. 2020.
[34] A. M. Rajab and B. Wang, "Automatic radio map database maintenance and updating based on crowdsourced samples for indoor localization," *IEEE Sensors J.*, vol. 22, no. 1, pp. 575–588, Jan. 2022.
[35] R. K. Sharma and J. W. Wallace, "Indoor shadowing correlation measurements for cognitive radio studies," in *Proc. IEEE Antennas Propag. Soc. Int. Symp.*, Jun. 2009, pp. 1–4.
[36] J. Liberti and T. Rappaport, "Statistics of shadowing in indoor radio channels at 900 and 1900 MHz," in *Proc. MILCOM Conf. Rec.*, vol. 3, 1992, pp. 1066–1070.
[37] MLIT Japan. *Project PLATEAU*. Accessed: Oct. 25, 2022. [Online]. Available: https://www.mlit.go.jp/plateau/
[38] National Research Foundation. *Virtual Singapore*. Accessed: Oct. 25, 2022. [Online]. Available: https://www.nrf.gov.sg/programmes/virtual-Singapore
[39] City of Helsinki. *Helsinki's 3D City Models*. Accessed: Oct. 25, 2022. [Online]. Available: https://www.hel.fi/helsinki/en/administration/information/general/3d/
[40] T. Nishio, H. Okamoto, K. Nakashima, Y. Koda, K. Yamamoto, M. Morikura, Y. Asai, and R. Miyatake, "Proactive received power prediction using machine learning and depth images for mmWave networks," *IEEE J. Sel. Areas Commun.*, vol. 37, no. 11, pp. 2413–2427, Nov. 2019.
[41] H. Iimori, G. T. F. de Abreu, O. Taghizadeh, R.-A. Stoica, T. Hara, and K. Ishibashi, "Stochastic learning robust beamforming for millimeter-wave systems with path blockage," *IEEE Wireless Commun. Lett.*, vol. 9, no. 9, pp. 1557–1561, Sep. 2020.
[42] K. S. Arun, T. S. Huang, and S. D. Blostein, "Least-squares fitting of two 3-D point sets," *IEEE Trans. Pattern Anal. Mach. Intell.*, vol. PAMI-9, no. 5, pp. 698–700, Sep. 1987.
[43] S. Choi, Q.-Y. Zhou, and V. Koltun, "Robust reconstruction of indoor scenes," in *Proc. IEEE Conf. Comput. Vis. Pattern Recognit. (CVPR)*, Jun. 2015, pp. 5556–5565.
[44] R. Hulik, M. Spanel, P. Smrz, and Z. Materna, "Continuous plane detection in point-cloud data based on 3D Hough transform," *J. Vis. Commun. Image Represent.*, vol. 25, no. 1, pp. 86–97, Jan. 2014.
[45] J. Schuster and R. Luebbers, "Comparison of site-specific radio propagation path loss predictions to measurements in an urban area," in *IEEE Antennas Propag. Soc. Int. Symposium. Dig.*, vol. 2, Jul. 1996, pp. 1210–1213.
[46] R. J. Luebbers, "Finite conductivity uniform GTD versus knife edge diffraction in prediction of propagation path loss," *IEEE Trans. Antennas Propag.*, vol. AP-32, no. 1, pp. 70–76, Jan. 1984.
[47] P. D. Holm, "A new heuristic UTD diffraction coefficient for nonperfectly conducting wedges," *IEEE Trans. Antennas Propag.*, vol. 48, no. 8, pp. 1211–1219, Aug. 2000.
[48] R. G. Kouyoumjian and P. H. Pathak, "A uniform geometrical theory of diffraction for an edge in a perfectly conducting surface," *Proc. IEEE*, vol. 62, no. 11, pp. 1448–1461, Nov. 1974.
[49] Y. Chen, Y. Li, C. Han, Z. Yu, and G. Wang, "Channel measurement and ray-tracing-statistical hybrid modeling for low-terahertz indoor communications," *IEEE Trans. Wireless Commun.*, vol. 20, no. 12, pp. 8163–8176, Dec. 2021.
[50] S. Bakirtzis, J. Chen, K. Qiu, J. Zhang, and I. Wassell, "EM DeepRay: An expedient, generalizable, and realistic data-driven indoor propagation model," *IEEE Trans. Antennas Propag.*, vol. 70, no. 6, pp. 4140–4154, Jun. 2022.
[51] K. Preusser and A. Schmeink, "Robust channel modeling of 2.4 GHz and 5 GHz indoor measurements: Empirical, ray tracing, and artificial neural network models," *IEEE Trans. Antennas Propag.*, vol. 70, no. 1, pp. 559–572, Jan. 2022.
[52] N. A. C. Cressie, *Statistics for Spatial Data*. Hoboken, NJ, USA: Wiley, 1993.
[53] A. E. Gelfand, P. Diggle, P. Guttorp, and M. Fuentes, *Handbook of Spatial Statistics*. Boca Raton, FL, USA: CRC Press, 2010.
[54] W. Jung, J. Hyeon, and N. Doh, "Robust cuboid modeling from noisy and incomplete 3D point clouds using Gaussian mixture model," *Remote Sens.*, vol. 14, no. 19, p. 5035, Oct. 2022. [Online]. Available: https://www.mdpi.com/2072-4292/14/19/5035
[55] W. Burside and K. Burgener, "High frequency scattering by a thin lossless dielectric slab," *IEEE Trans. Antennas Propag.*, vol. AP-31, no. 1, pp. 104–110, Jan. 1983.

NORISATO SUGA (Member, IEEE) received the B.E., M.E., and Ph.D. degrees from the Faculty of Engineering, Tokyo University of Science, Tokyo, Japan, in 2011, 2013, and 2016, respectively. From 2016 to 2019, he was a Researcher with the Advanced Telecommunications Research Institute International (ATR). From 2019 to 2022, he was an Assistant Professor with the Faculty of Engineering, Tokyo University of Science. Since 2022, he has been an Assistant Professor with the Faculty of Information and Communications Engineering, Shibaura Institute of Technology. His current research interests include digital signal processing for wireless communication and quality prediction of wireless communication systems. He received the ISPACS 2019 Best Paper Award.

YOSHIHIRO MAEDA (Member, IEEE) received the B.E., M.E., and Ph.D. degrees in information engineering from the Nagoya Institute of Technology, Japan, in 2013, 2015, and 2019, respectively. He became an Assistant Professor with the Tokyo University of Science, Japan, in 2019. His research interests include image processing and multispectral sensing.

KOYA SATO (Member, IEEE) was born in Miyagi, Japan, in 1991. He received the B.E. degree in electrical engineering from Yamagata University, in 2013, and the M.E. and Ph.D. degrees from The University of Electro-Communications, in 2015 and 2018, respectively. From 2018 to 2021, he was an Assistant Professor with the Tokyo University of Science. He is currently an Assistant Professor with the Artificial Intelligence eXploration Research Center, The University of Electro-Communications. His current research interests include wireless communication, distributed machine learning, and spatial statistics.